Tuning the Structural Rigidity of Two-Dimensional Ruddlesden-Popper Perovskites through the Organic Cation

Fridriksson, Magnus B.; Van Der Meer, Nadia; De Haas, Jiska; Grozema, Ferdinand C.

DOI
10.1021/acs.jpcc.0c08893

Publication date
2020

Document Version
Final published version

Published in
Journal of Physical Chemistry C

THE JOURNAL OF PHYSICAL CHEMISTRY C

pubs.acs.org/JPCC

Article

Tuning the Structural Rigidity of Two-Dimensional Ruddlesden–Popper Perovskites through the Organic Cation

Magnus B. Fridriksson, Nadia van der Meer, Jiska de Haas, and Ferdinand C. Grozema*

Cite This: J. Phys. Chem. C 2020, 124, 28201–28209

Read Online

ACCESS | Metrics & More | Article Recommendations | Supporting Information

ABSTRACT: Two-dimensional (2D) hybrid organic–inorganic perovskites are an interesting class of semi-conducting materials. One of their main advantages is the large freedom in the nature of the organic spacer molecules that separates the individual inorganic layers. The nature of the organic layer can significantly affect the structure and dynamics of the 2D material; however, there is currently no clear understanding of the effect of the organic component on the structural parameters. In this work, we have used molecular dynamics simulations to investigate the structure and dynamics of a 2D Ruddlesden–Popper perovskite with a single inorganic layer (n = 1) and varying organic cations. We discuss the dynamic behavior of both the inorganic and the organic part of the materials as well as the interplay between the two and compare the different materials. We show that both aromaticity and the length of the flexible linker between the aromatic unit and the amide have a clear effect on the dynamics of both the organic and the inorganic part of the structures, highlighting the importance of the organic cation in the design of 2D perovskites.

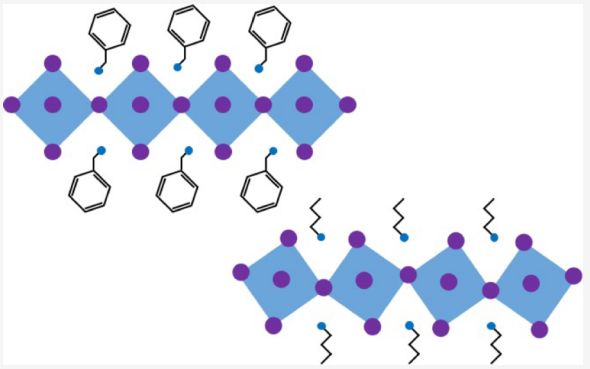

INTRODUCTION

In recent years, two-dimensional (2D) Ruddlesden–Popper hybrid halide perovskite materials have attracted interest as optoelectronic materials,[1−3] in particular as a more stable alternative for their three-dimensional (3D) counterparts.[4,5] The use of 2D perovskites has already been demonstrated in light-emitting diodes (LED),[6,7] lasers,[8,9] and solar cell devices[10−12] with good results. The general structure of 2D Ruddlesden–Popper perovskites is $(R\text{-}NH_3)_2A_{n-1}B_nX_{3n+1}$,[13,14] where B and X are a metal cation and a halide, respectively; A is a small (organic) cation incorporated in the cavities of the metal halide lattice, and R is a larger organic amide, which is responsible for breaking the perovskite structure into 2D layers.[15,16]

One of the main advantages of the 2D Ruddlesden–Popper perovskites compared to 3D perovskites is the added design freedom introduced by the large organic cation. As is the case with 3D perovskites, it is possible to vary the A, B, and X ions, which affects the electronic properties of the material.[3,17,18] However, for 2D perovskites, there is an added freedom in choosing the large organic cation ($R\text{-}NH_3$) where specific functional organic moieties can be introduced. In addition, the number of inorganic layers (n) in the structure can be varied by changing the ratio between the small (A) and large organic cations. Altering these variables affects several properties of the material. For instance, the number of inorganic layers has been shown to affect the band gap[19] as well as both the exciton binding energy[20] and the exciton diffusion length.[21] Additionally, changes in the structure of the large organic cation have been shown to affect the dielectric environment,[22,23] electron–phonon coupling,[24] the stability of the perovskite toward air and moisture,[25] and the exciton diffusion length.[26]

Currently, the most common large organic cations for 2D Ruddlesden–Popper perovskites are n-butylammonium (BA)[13,19,27] and phenylethylammonium (PEA).[6,28,29] They differ in the sense that PEA contains an aromatic phenyl group that can aid in the packing of the organic molecules through $\pi-\pi$ interactions. 2D perovskites with a variety of larger organic cations have also been made, including longer aliphatic chains such as hexyl- and octylammonium[30−32] and large conjugated molecules.[25,33−35] These larger conjugated molecules exhibit even stronger $\pi-\pi$ interactions than PEA and have been shown to result in exceptional moisture stability.[25]

The effects of changes in the organic component are known to be very subtle, and depending on the nature of the organic component and the processing conditions, often lower-dimensional structures are formed.[36,37] In addition, the interaction between the organic moieties in the side chains

Received: September 30, 2020
Revised: November 22, 2020
Published: December 14, 2020

https://dx.doi.org/10.1021/acs.jpcc.0c08893
J. Phys. Chem. C 2020, 124, 28201–28209

can have a distinct effect on the structure and dynamics of the inorganic layers in the material and in this way can indirectly affect the optoelectronic properties of the material. A detailed understanding of the interplay between the interactions in the layer of large organic cations and the inorganic layer is essential in the design of new 2D perovskite materials. However, at present, the understanding of these interactions is currently very limited, especially since theoretical studies of the structural dynamics are largely limited to BA, PEA, and some small organic cations. It is especially interesting to consider the effect of the aromaticity and the length of an aliphatic chain on the structure and dynamics of the inorganic layer. A large aromatic core will have stronger $\pi-\pi$ interactions resulting in the molecules packing closer together and moving less, which could influence the motion of the inorganic layer and make it more rigid. However, the length of the aliphatic chain could also play a role as a longer chain can result in more movement independent of the aromaticity.

In this work, we have performed classical molecular dynamics (MD) simulations on n = 1 Ruddlesden−Popper perovskites with a lead−iodideinorganic layer and three different organic cations varying in the presence and size of the aromatic component and in the length of the aliphatic chain connected to the amide. The organic cations considered are BA, PEA, and pyrene-*o*-butylammonium (POB). We then compare the dynamics of the organic molecules and the dynamics and structure of the inorganic lead−iodide layer and discuss the interplay between these two parts. We show that both the aromaticity and the length of the aliphatic chain have a substantial effect on the structure and dynamics of both the organic and the inorganic part of the system, highlighting the impact the organic cations can have on the properties of 2D perovskites.

METHODS

The MD simulations were performed using the LAMMPS software.[38] A time step of 1 fs was used for all the simulations, and all the simulations started at 300 K, where the system was equilibrated for 1 ns. Thereafter, the temperature was decreased to the desired temperature with a fixed annealing rate of 125 K/ns. When the desired temperature was reached, the system was again allowed to equilibrate for 1 ns before a 100 ps production run was performed. Throughout the production run, the positions of all the atoms were recorded.

The force field used in the MD simulations was based on the MYP force field[39] and on our previous work on 3D perovskites[40] and 2D Ruddlesden−Popper perovskites with a varying number of inorganic layers where BA was taken as the large organic cation.[41] The intermolecular potential for lead and iodide was taken from the MYP force field[39] and consisted of a Buckingham potential, except for the interaction between either lead or iodide with hydrogen where a Lennard-Jones potential was used. Both the inter- and intramolecular parameters for BA were the same as in our previous work,[41] while the additional parameters for PEA and POB were obtained from the standard Amber force field,[42] consistent with the MYP force field. All intermolecular interactions between two organic molecules were described by a Lennard-Jones potential. To make the force field transferable between the different materials that we consider, we deviated from the MYP force field in one respect: the partial charges for the Coulomb interactions. We assigned the full formal charges +2 and −1 to the lead and iodide ions (versus +2.02 and −1.13 in the MYP force field). In addition, the organic cations had a full +1 charge that was distributed over all atoms, as obtained from an electronic structure calculation. The partial charges on the individual atoms in the organic molecules were obtained by fitting them to the electrostatic potential from a density functional theory calculation (B3LYP/cc-pVTZ) using the CHelpG approach[43] in the Gaussian09 software.[44] To confirm that the force field described above reproduced the experimental structure, we compared the average unit cell dimensions (a, b, and c) for simulations at 300 K with the literature values (the values used for the initial structures) for each material in Table 1. The unit cell angles were not included as these were not modified during the simulation. As can be seen, the average dimensions are in all cases slightly larger (from 2.6% for BA to 6.6% for PEA) than the crystal structure values, but the agreement is satisfactory, especially since we use a transferable force field that is not optimized for each material separately.

Table 1. Comparison of Average Unit Cell Dimensions (in Å) during Simulations at 300 K and the Literature Values Used for the Initial Structures

organic molecule	parameter	a	b	c
BA	average dimension (Å)	8.9152	9.1180	28.363
	literature value (Å)	8.6918	8.8895	27.652
	percentage difference	2.6%	2.6%	2.6%
PEA	average dimensions (Å)	9.3187	9.3202	35.184
	literature value (Å)	8.7389	8.7403	32.9952
	percentage difference	6.6%	6.6%	6.6%
POB	average dimensions (Å)	55.951	6.4792	13.189
	literature value (Å)	53.3048	6.1727	12.565
	percentage difference	5.0%	5.0%	5.0%

The initial structures were obtained from the experimental crystal structures of the materials.[14,28,33] The MD box consists of a supercell of 10 × 10 unit cells in the in-plane directions. In the direction perpendicular to the inorganic lead−iodide layer, only a single unit cell was used since the unit cell already contained two layers of lead and iodide, ensuring that there was no direct interaction with the same layer. Periodic boundary conditions were used in all directions, and the NPT ensemble was used, with a Nose−Hoover thermo- and barostat.[45] The cutoff used for electrostatic interactions was less than half of the simulation box size in the smallest direction to avoid artificial periodic electrostatic coupling, with long-range effects taken into account using the Ewald method.[45]

RESULTS AND DISCUSSION

To analyze how the intermolecular interactions in the organic part of the material affect the dynamics in 2D Ruddlesden−Popper perovskites, we analyze the MD trajectories of the materials at different temperatures. The analysis is separated into three parts. We first discuss the dynamics of the organic part after which we consider the structure and dynamics of the inorganic layer. Finally, we examine the interaction between the organic molecules and the inorganic layer.

Dynamics of the Organic Molecules. In Figure 1, the three large organic cations considered in this work are shown. As can be seen, the molecular structures vary considerably,

https://dx.doi.org/10.1021/acs.jpcc.0c08893
J. Phys. Chem. C 2020, 124, 28201−28209

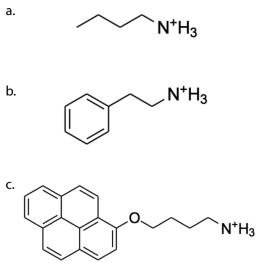

Figure 1. Large organic cations present in the examined structures. (a) *n*-Butylammonium (BA). (b) Phenylethylammonium (PEA). (c) Pyrene-*o*-butylammonium (POB).

leading to differences in the interaction. The structural differences make it also challenging to compare their dynamics. A common structural element in all compounds is the amide group that coordinates with the inorganic layer. An obvious way to monitor the motion of this linking amide group is to compare the rotational dynamics of the C−N bond in the amide group in the different molecules. This is achieved by comparing the rotational autocorrelation function (ACF) of the C−N bond for the different materials. The rotational autocorrelation function is calculated according to the following equation where N_{ion} is the number of organic cations, N_{t0} is the number of initial times (t_0) considered, and $\hat{n}$ is the unit vector in the direction of the bond.

$$A(t) = \langle \hat{n}(t)\cdot\hat{n}(0)\rangle = \frac{1}{N_{ion}}\sum_{i}\frac{1}{N_{t0}}\sum_{t_1=t+t_0}\hat{n}_i(t_1)\cdot\hat{n}_i(t_0)$$

The ACF gives an indication of the extent of the rotational motion of the bond and of the time scale on which this motion occurs. Initially, the ACF is always equal to 1, but as a function of time, it will decay as the average direction of the bond will start to deviate from the initial direction. For a freely rotating bond, the ACF will decay to zero eventually, indicating a random orientation on average. If the rotational motion is restricted, then the ACF does not decay all the way to zero but a plateau may be reached after some time. Such restricted motion is found in the rotational dynamics in the present case since the coordination of the amide group to the inorganic layer prevents full reorientation of the C−N bond. Therefore, a plateau value is reached after some time. Higher plateau values indicate a more restricted rotational motion of the bond compared to lower ones. The time required to reach the plateau indicates the time scale on which the rotational motion takes place and can be defined as a rotational diffusion time. In Figure 2, the ACF of the C−N bond is shown for the three compounds at all simulated temperatures.

From Figure 2a, we can see that, at high temperatures (300 K), the ACF reaches a plateau with a significantly higher value for PEA than for the other two molecules, indicating a more restricted rotational freedom for the C−N bond. This indicates a more rigid structure that is likely to be related to the combination of $\pi-\pi$ interactions and the short relatively rigid ethyl linker. BA and POB seem to reach a similar value after 100 ps, although for POB, no plateau is reached within the 100 ps simulation time. It is obvious that the rotational diffusion of the C−N bond in BA is considerably faster than in BOP as its ACF decays rapidly within the first 10 ps after which it stays constant. This difference in the time scale of the rotation can be attributed to the large bulky aromatic part of POB that

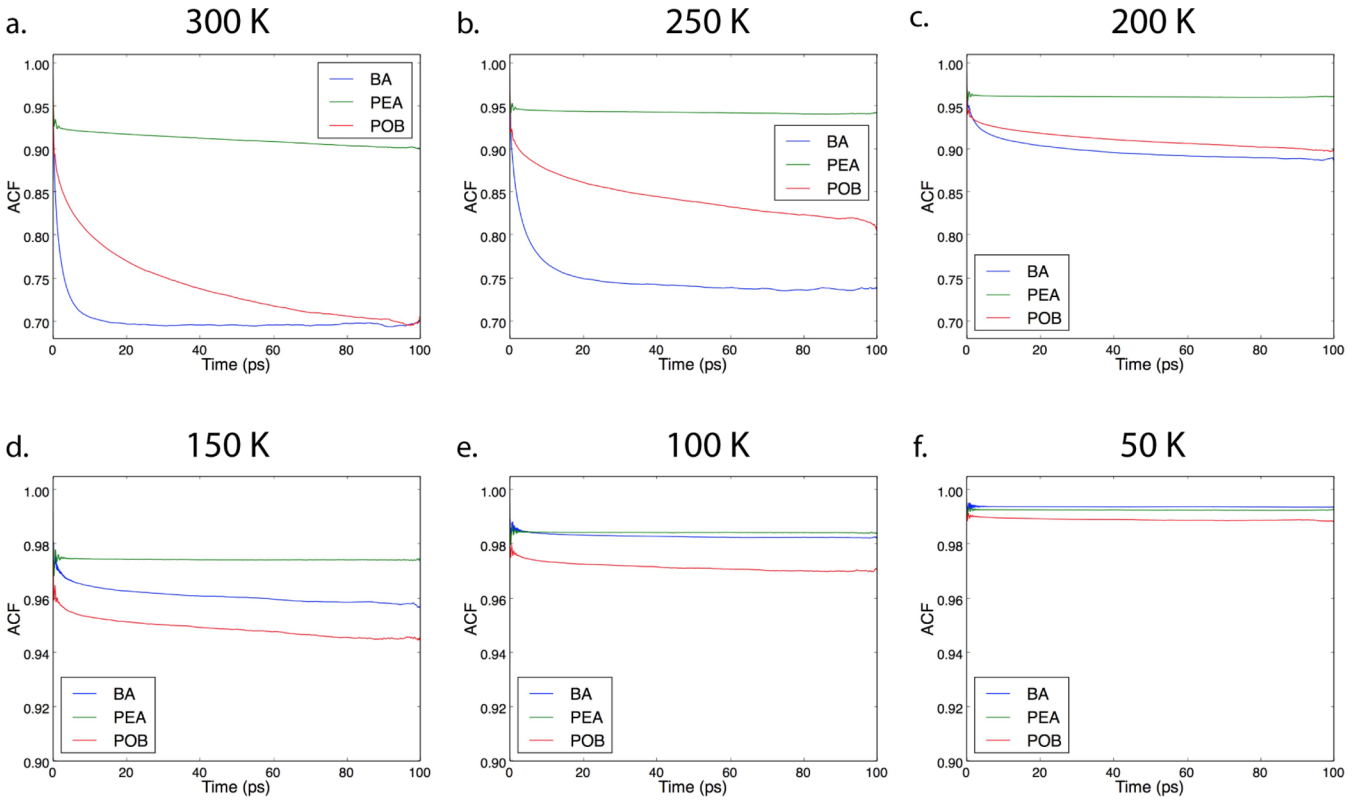

Figure 2. Rotational autocorrelation function of the C−N bond in the three organic molecules at different temperatures. (a) 300 K. (b) 250 K. (c) 200 K. (d) 150 K. (e) 100 K. (f) 50 K.

https://dx.doi.org/10.1021/acs.jpcc.0c08893
J. Phys. Chem. C 2020, 124, 28201−28209

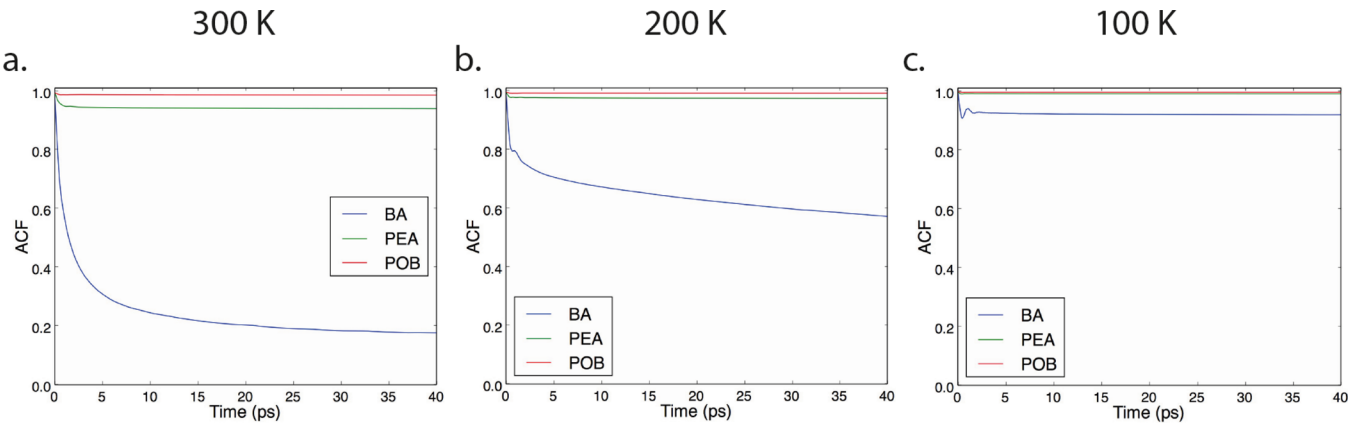

Figure 3. Rotational autocorrelation function of the end C−C bond in BA and the vector across a phenyl group in PEA and POB. (a) 300 K. (b) 200 K. (c) 100 K.

slows down the rotational movement of the C−N bond in POB.

As the temperature is lowered, the overall decay in the ACF is less for all compounds, indicating a more rigid structure. For all temperatures, the motion of the C−N bond in PEA remains the most restricted, apart from the simulations at 50 K (Figure 2f) where BA has a slightly higher ACF plateau. However, at this temperature, the ACF values remain close to 1.0 for both molecules, indicating that the bond is more or less fixed in both cases. In the case of POB, the bond rotation gradually becomes less as the temperature is lowered, as reflected in the higher ACF values. The time scale of the rotation remains slow, as can be seen from the lack of plateau formation for POB at all temperatures within the 100 ps simulation time.

For BA, the decay of the ACF at 250 K (Figure 2b) is similar to the behavior at 300 K, apart from a slightly higher plateau value. When the temperature is lowered further to 200 K (Figure 2c), a large change in the decay of the ACF is observed, including a slower day and a considerably higher plateau value. This indicates reduced rotational motion of the C−N bond in BA, which is consistent with the occurrence of a phase transition in the material. This agrees well with the experimentally known phase transition that occurs in this material in the same temperature interval.[30] As the temperature is lowered further, the ACF plateau value of BA becomes substantially higher than that of POB and reaches a value similar to PEA.

To gain insight in the motion in the other parts of the organic layer, we also consider the rotation of bonds further away from the amide group. In Figure 3, the rotational ACFs of the aromatic units in PEA and POB (defined by a vector through a phenyl group along the axis of the aromatic part) are compared with the rotation of the terminal C−C bond in BA. Not surprisingly, the terminal C−C bond in BA has substantial rotational freedom at all temperatures, although the motion is strongly restricted at low temperature. In contrast, the $\pi-\pi$ interactions in PEA and POB lead to a rigidly packed structure at all temperatures with ACF values very close to 1. Comparison of the ACF for PEA and POB shows that the rotation of the aromatic part of POB is even more restricted than that of PEA as a result of the large aromatic unit. Overall, this shows that more rigid tightly packed organic layers are formed when large aromatic units are attached to the amide. The formation of such a tightly packed layer isolates that inorganic part from moisture, explaining the exceptional moisture stability of the POB compounds reported experimentally.[33] The extent to which the rigidity of the organic layer is transmitted to the amide group that connects with the inorganic layer depends strongly on the linker. For the short relatively rigid ethyl linker in PEA, this results in a severely restricted rotational motion of the C−N bond, while the longer flexible linker in POB allows a rotational freedom comparable to BA.

Structure and Dynamics of the Inorganic Lead−Iodide Layer. To investigate the rigidness of the lead−iodide layer in the different structures, we analyze how much lead atoms deviate from the lead−iodide layer plane throughout the simulation. A detailed description of the procedure followed can be found in the Supporting Information. The standard deviation of the lead atoms with respect to the lead−iodide layer plane is shown as a function of temperature in Figure 4.

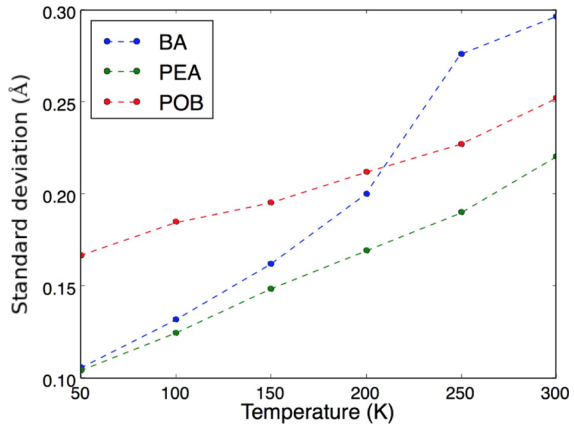

Figure 4. Standard deviation of lead atom deviation from the lead plane.

From Figure 4, it is clear that, at all temperatures, the lead atoms in the PEA structure deviate the least from the lead−iodide plane. At high temperatures, the BA structure exhibits the largest deviation, but between 250 and 200 K, it drops drastically. This is the same temperature range as where a sudden jump in the ACF decays for BA was observed, consistent with the claim that this is related to a phase transition in the material. The deviation of the lead atoms in the POB structure decreases gradually as the temperature is lowered similar to PEA. However, the deviation is substantially

https://dx.doi.org/10.1021/acs.jpcc.0c08893
J. Phys. Chem. C 2020, 124, 28201−28209

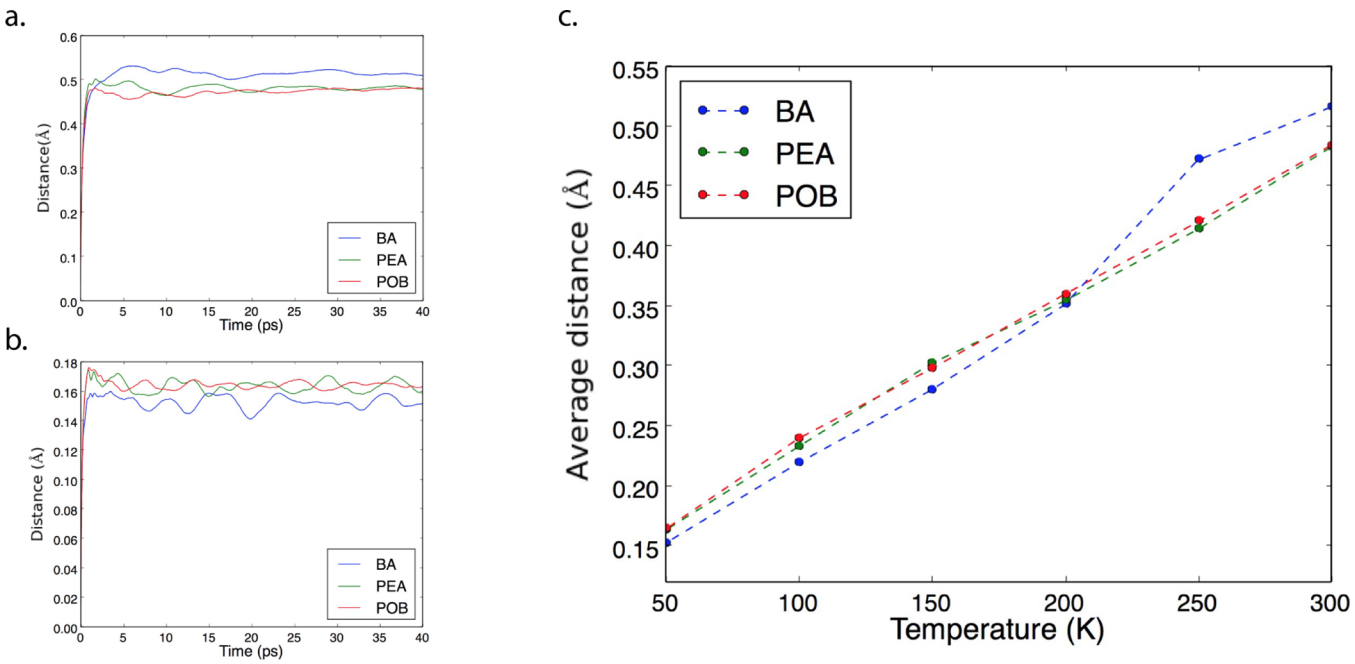

Figure 5. (a, b) Average distance of the lead atom from its position at t = 0 versus time at (a) 300 and (b) 50 K. (c) Average distance in the range of 10−100 ps versus temperature.

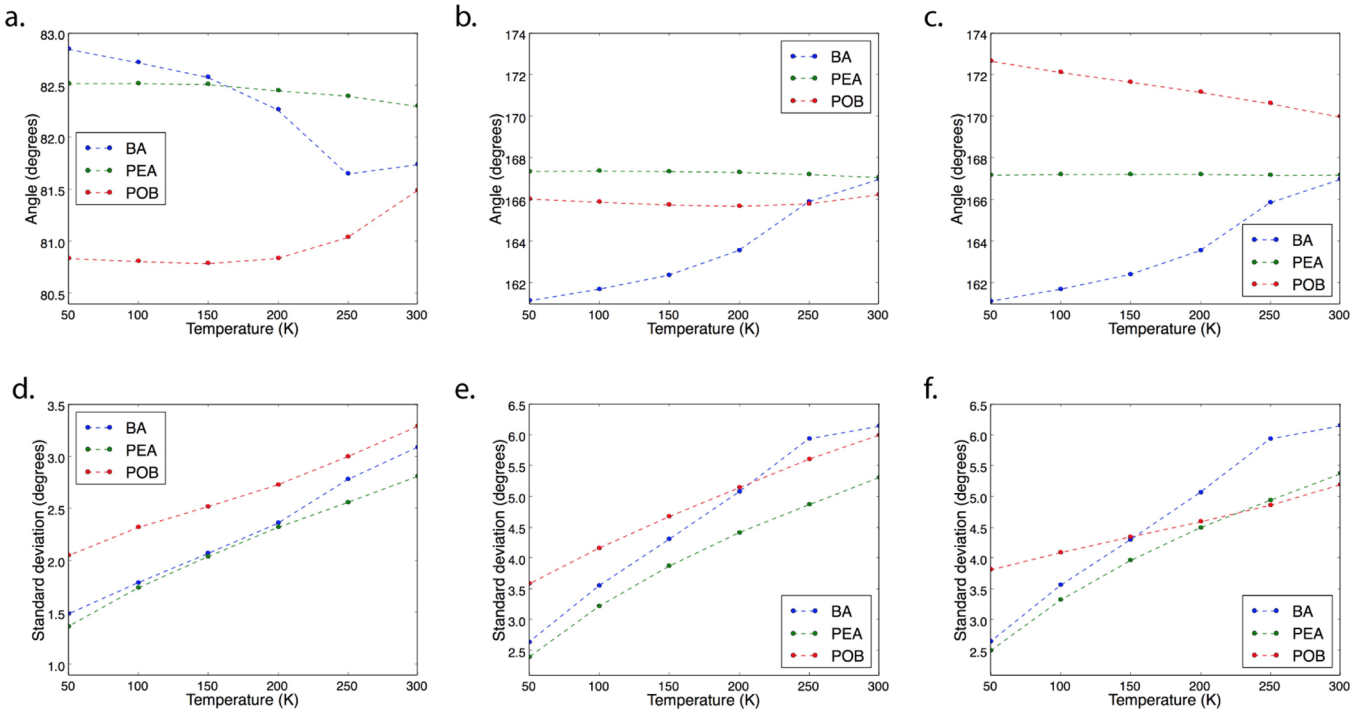

Figure 6. Out-of-layer iodide and Pb−I−Pb angles for all structures versus temperature. (a) Average out-of-layer iodide angles. (b) Average Pb−I−Pb angles in the x direction. (c) Average Pb−I−Pb angles in the y direction. (d) Standard deviation of the out-of-layer iodide angles. (e) Standard deviation of the Pb−I−Pb angles in the x direction. (f) Standard deviation of the Pb−I−Pb angles in the y direction.

larger in the case of POB, indicating that the lead atoms are less restricted in the lead−iodide plane.

For a more detailed picture of the dynamics of the inorganic lead−iodide layer, we have calculated the average absolute distance of a lead atom from its position at a certain reference time (t_0) as a function of time in all directions. This movement is shown in Figure 5a and Figure 5b for 300 and 50 K, respectively. In Figure 5c, the mean absolute distance averaged over the time range of 10−100 ps is plotted as a function of temperature. These curves give an indication of the fluctuations in the position of the Pb atoms, independent on the direction of the movement.

Figure 5c shows that the lead atoms in the BA structure have the largest freedom to move around at high temperatures (250 and 300 K). However, lowering the temperature from 250 to 200 K results in a sharp decrease in movement. At all

https://dx.doi.org/10.1021/acs.jpcc.0c08893
J. Phys. Chem. C 2020, 124, 28201−28209

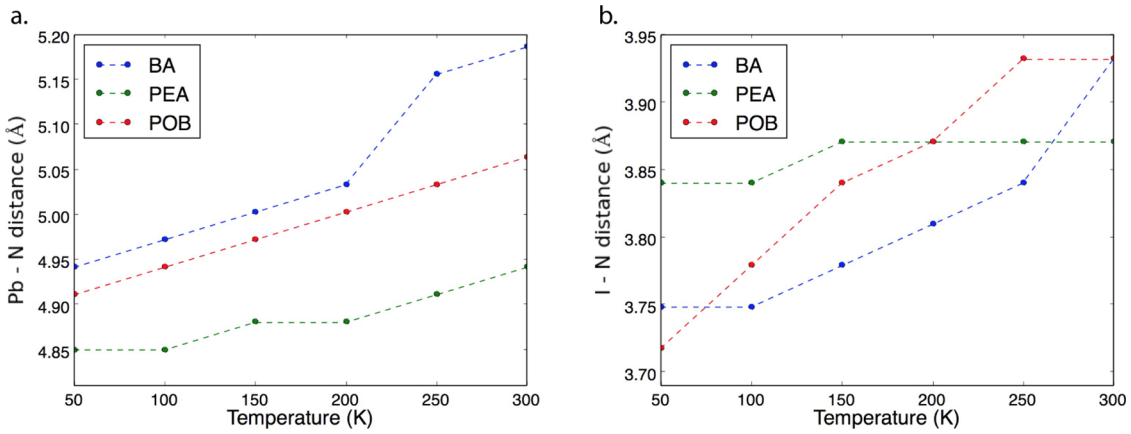

Figure 7. Positions of the first RDF peak for (a) lead and nitrogen and (b) iodide and nitrogen.

temperatures below 200 K, the lead atoms in the BA structure have the least freedom to move. This is consistent with the occurrence of a phase transition in the BA material between 250 and 200 K, resulting in a more rigid structure.

Interestingly, the PEA structure and the POB structure show more or less identical mean average movement for the ions at all temperatures. This is in contrast to the observations above for the movement of the Pb ions out of the inorganic plane. A substantially higher out-of-plane movement was found for the POB structure than for the PEA structure. This indicates that the overall movement is similar in both structures, but that in the PEA structure, the out-of-plane motion is significantly reduced, as compared to the POB material.

To obtain a more detailed insight in the structural fluctuations in the different 2D perovskite materials, we have examined the tilting of the inorganic octahedra in two different directions. First, we examine the Pb−I−Pb angles within each lead−iodide layer. The Pb−I−Pb angle corresponds to the mutual angle between two neighboring octahedra and will therefore give an indication of the tilting of the octahedra in each structure. It is defined in the range of 0−180°, where 180° corresponds to a perfectly cubic structure. Increased tilting of the octahedra results in a lower Pb−I−Pb angle. We distinguish between the two different directions of the Pb−I−Pb angles within the layer since these are not necessarily the same. The materials considered in this work all consist of a single inorganic layer flanked between organics (n = 1); hence, there is no Pb−I−Pb angle in the direction perpendicular to the inorganic layer. To gain insight in the tilting of the octahedra with respect to the inorganic plane, we also examine the out-of-layer iodide angle. The out-of-layer iodide angle is the angle between the lead−iodide layer plane and a vector between the two iodides in the octahedra that are above and below the plane. The out-of-layer iodide angle is defined in the range of 0−90°. If the structure is perfectly cubic, then the out-of-layer iodide angle will be 90°, but any tilting of the octahedra will result in a smaller angle. In Figure 6, the averages and standard deviations of both the out-of-layer iodide angles and the Pb−I−Pb angles are shown.

From Figure 6a−c, it is clear that the octahedral tilting in the PEA material is virtually unaffected by temperature in all directions, indicating that no significant structural changes take place as the temperature is lowered. In the case of the BA structure, structural changes are observed in all three angles as the temperature decreases from 250 to 200 K. The out-of-layer iodide angle increases, indicating less tilting of the octahedra in that direction, while the Pb−I−Pb angles decrease in both the x and y direction in a similar way, indicating increased tilting of the octahedra in the layer. This change in the octahedral tilting is consistent with our previous notions that we observe a phase transition in the material between these temperatures. The POB structure also exhibits some structural changes, but they differ from what was observed for the BA structure. In this case, the out-of-layer iodide angle decreases as the temperature is lowered from 300 down to 200 K and remains fairly constant below that. It should also be noted that the POB structure has the smallest out-of-layer iodide angle at all temperatures and therefore the largest octahedral tilt in that particular direction. The Pb−I−Pb angle in the x direction for the POB structure hardly changes with temperature, while the same angle in the y direction increases gradually as the temperature is decreased. The standard deviation of the out-of-layer iodide angles and the Pb−I−Pb angles decreases steadily as the temperature is lowered for all the different structures, as expected.

If we compare the three different structural parameters related to the inorganic lead−iodide layer considered here, then there will be some interesting observations. Even though the lead atoms have similar freedom to move in the structures containing PEA and POB, POB exhibits more movement in the direction perpendicular to the lead−iodide layer. The POB compounds also shows substantially more tilting of the octahedra than the PEA structure in that particular direction. This indicates that there is a relation between the tilting of the octahedra in the direction perpendicular to the lead−iodide layer and the rigidity of the same layer. Structures with less-tilted octahedra (closer to a cubic structure) result in reduced motion of the lead atoms perpendicular to the inorganic layer.

Interactions between the Organic and the Inorganic Part of the System. In the preceding two sections, we have separately considered the structural dynamics in the organic and the inorganic parts. However, these two parts of the materials are intimately connected. Therefore, we now turn to the interaction between the organic and the inorganic parts. The connection of the two components is formed by the ionic bonding between the amide unit and the Pb−I framework. Some structural insights of this interaction can be derived from the radial distribution function for both lead and nitrogen and iodide and nitrogen, as shown in Figures S2 and S3 at 300 and 50 K. The lead−nitrogen RDF gives information about the proximity of the amide unit of organic molecules and the lead atoms in the inorganic layers. The amide unit "fills" the cavity formed by the inorganic octahedra and can therefore be

https://dx.doi.org/10.1021/acs.jpcc.0c08893
J. Phys. Chem. C 2020, 124, 28201−28209

interpreted as a penetration depth of the organic molecule into the inorganic layer. The iodide−nitrogen RDF is related to the distance between the amide and iodide and can be seen as an indication of whether hydrogen bonds are formed between iodide and the amide hydrogens.

To ease the comparison of the RDFs at different temperatures for the different materials, we show in Figure 7 the position of the first RDF peak versus temperature for the three materials. This gives an indication of the nearest neighbor distances between lead and nitrogen and iodide and nitrogen. From Figure 7a, we see that the Pb−N distance is the highest for the BA material at all temperatures and we can again see the effect of phase transition occurring in the BA structure as the temperature is lowered from 250 to 200 K. During this phase transition, the lead−nitrogen distance decreases substantially, indicating a more tight incorporation of the amide in the cavities in the inorganic structure (or a larger penetration). For the PEA and POB materials, no sudden drop in the Pb−N distance is observed but they do show a gradual decrease in the distance with temperature. It is worth noting that the PEA structure exhibits a significantly smaller Pb−N distance at all temperatures but particularly at 300 K. This shows that the average penetration of the amide in PEA is the largest.

The iodide−nitrogen distance shown in Figure 7b in the PEA structure is more or less stable over all the simulated temperatures, while for the structures including BA and POB, there is a steady decrease as the temperature is lowered. This difference can be explained by the difference in the aliphatic chain length of the organics. BA and POB both have four carbons in their chain, while PEA only has two. The longer the aliphatic chain, the more freedom the nitrogen has to approach iodide to form hydrogen bonds, resulting in the shorter distance at low temperatures.

General Discussion. The analysis above shows that the structural dynamics in 2D Ruddlesden−Popper perovskites are considerably affected by the nature of the organic component. The nature of the organic group connected to the amide does not only affect the organic layer, but also significantly affects the inorganic layer. For the BA compound, this is clear in the phase transitions that take place in the materials. This phase transition leads to structural rearrangements in the inorganic layer, which is accompanied by a reduced rotational motion of the BA cation and a larger penetration of the amide into the inorganic layer. Introduction of an aromatic unit in the organic layer leads to substantially reduced structural fluctuations there. This reduction in fluctuations is transmitted to the inorganic layer when the aromatic unit is coupled to the amide with a short rigid linker such as ethyl in the PEA-based material. This is consistent with experimental observations of the differences in structural rigidity between PEA and BA.[26,46] When the length of the linker is increased such as in the POB compound, the flexibility of the amide is increased, but the rigidity of the aromatic part of the material is maintained. The latter leads to a strongly enhanced resistance to moisture while leaving the structural rigidity of the inorganic part unaffected. These observations have some interesting implications for the design of 2D halide perovskites. The results show that the structural softness of alkyl-based perovskites can be overcome by introducing aromatic side chains; however, the linker between the aromatic unit and the amide plays an important role in this. A short linker can transmit this increased rigidity to the inorganic framework, while a longer flexible linker will allow for substantial fluctuations in the inorganic part.

CONCLUSIONS

In this work, we show that the nature of the organic component has a marked effect on the structural rigidity of 2D Ruddlesden−Popper perovskites. Both the aromaticity of the organic component and the length of the aliphatic linker connecting it to the amine have a large influence on the structure and dynamics of the materials. Introduction of aromatic units such as phenyl or pyrene in the organic component results in a more rigid organic layer. The length of the aliphatic linker significantly affects the motion of the amide group, with a longer chain allowing more movement. These effects are not only limited to the behavior of the organic molecule itself but also directly affect the inorganic layer. More rigidity in the organic part due to aromatic interactions combined with a short rigid linker leads to less dynamic inorganic layers such as in the PEA structure considered. The results presented indicate that there is a subtle interplay between interactions in the organic and the inorganic parts of the material and that different aspects of the organic component that is used should be considered when designing new 2D hybrid perovskites.

ASSOCIATED CONTENT

Supporting Information

The Supporting Information is available free of charge at https://pubs.acs.org/doi/10.1021/acs.jpcc.0c08893.

All the parameters used for the molecular dynamics force field (Tables S1−S16) with a figure explaining the atom numbering for charges (Figure S1), explanation of the lead atom deviation from the lead iodide plane, and the radial distribution functions at 50 and 300 K for both lead and nitrogen and iodide and nitrogen (Figures S2 and S3) (PDF)

AUTHOR INFORMATION

Corresponding Author

Ferdinand C. Grozema − *Department of Chemical Engineering, Faculty of Applied Sciences, Delft University of Technology, Delft 2629 HZ, The Netherlands;* orcid.org/0000-0002-4375-799X; Email: f.c.grozema@tudelft.nl

Authors

Magnus B. Fridriksson − *Department of Chemical Engineering, Faculty of Applied Sciences, Delft University of Technology, Delft 2629 HZ, The Netherlands*

Nadia van der Meer − *Department of Chemical Engineering, Faculty of Applied Sciences, Delft University of Technology, Delft 2629 HZ, The Netherlands*

Jiska de Haas − *Department of Chemical Engineering, Faculty of Applied Sciences, Delft University of Technology, Delft 2629 HZ, The Netherlands*

Complete contact information is available at: https://pubs.acs.org/10.1021/acs.jpcc.0c08893

Author Contributions

The manuscript was written through contributions of all authors. All authors have given approval to the final version of the manuscript.

https://dx.doi.org/10.1021/acs.jpcc.0c08893
J. Phys. Chem. C 2020, 124, 28201−28209

Notes

The authors declare no competing financial interest.

■ ACKNOWLEDGMENTS

The research leading to these results in the Delft University of Technology has received funding from the European Research Council Horizon 2020 ERC grant agreement no. 648433.

■ REFERENCES

(1) Chen, Y.; Sun, Y.; Peng, J.; Tang, J.; Zheng, K.; Liang, Z. 2D Ruddlesden−Popper Perovskites for Optoelectronics. *Adv. Mater.* **2018**, *30*, 1703487.
(2) Yan, J.; Qiu, W.; Wu, G.; Heremans, P.; Chen, H. Recent Progress in 2D/Quasi-2D Layered Metal Halide Perovskites for Solar Cells. *J. Mater. Chem. A* **2018**, *6*, 11063−11077.
(3) Quan, L. N.; Rand, B. P.; Friend, R. H.; Mhaisalkar, S. G.; Lee, T.-W.; Sargent, E. H. Perovskites for Next-Generation Optical Sources. *Chem. Rev.* **2019**, *119*, 7444−7477.
(4) Kim, J.; Ho-Baillie, A.; Huang, S. Review of Novel Passivation Techniques for Efficient and Stable Perovskite Solar Cells. *Sol. RRL* **2019**, *3*, 1800302.
(5) Krishna, A.; Gottis, S.; Nazeeruddin, M. K.; Sauvage, F. Mixed Dimensional 2D/3D Hybrid Perovskite Absorbers: The Future of Perovskite Solar Cells? *Adv. Funct. Mater.* **2019**, *29*, 1806482.
(6) Yuan, M.; Quan, L. N.; Comin, R.; Walters, G.; Sabatini, R.; Voznyy, O.; Hoogland, S.; Zhao, Y.; Beauregard, E. M.; Kanjanaboos, P.; et al. Perovskite Energy Funnels for Efficient Light-Emitting Diodes. *Nat. Nanotechnol.* **2016**, *11*, 872−877.
(7) Tsai, H.; Nie, W.; Blancon, J.-C.; Stoumpos, C. C.; Soe, C. M. M.; Yoo, J.; Crochet, J.; Tretiak, S.; Even, J.; Sadhanala, A.; et al. Stable Light-Emitting Diodes Using Phase-Pure Ruddlesden−Popper Layered Perovskites. *Adv. Mater.* **2018**, *30*, 1704217.
(8) Li, M.; Wei, Q.; Muduli, S. K.; Yantara, N.; Xu, Q.; Mathews, N.; Mhaisalkar, S. G.; Xing, G.; Sum, T. C. Enhanced Exciton and Photon Confinement in Ruddlesden-Popper Perovskite Microplatelets for Highly Stable Low-Threshold Polarized Lasing. *Adv. Mater.* **2018**, *30*, 1707235.
(9) Zhang, H.; Liao, Q.; Wu, Y.; Zhang, Z.; Gao, Q.; Liu, P.; Li, M.; Yao, J.; Fu, H. 2D Ruddlesden−Popper Perovskites Microring Laser Array. *Adv. Mater.* **2018**, *30*, 1706186.
(10) Tsai, H.; Nie, W.; Blancon, J. C.; Stoumpos, C. C.; Asadpour, R.; Harutyunyan, B.; Neukirch, A. J.; Verduzco, R.; Crochet, J. J.; Tretiak, S.; et al. High-Efficiency Two-Dimensional Ruddlesden-Popper Perovskite Solar Cells. *Nature* **2016**, *536*, 312−316.
(11) Cao, D. H.; Stoumpos, C. C.; Yokoyama, T.; Logsdon, J. L.; Song, T.-B.; Farha, O. K.; Wasielewski, M. R.; Hupp, J. T.; Kanatzidis, M. G. Thin Films and Solar Cells Based on Semiconducting Two-Dimensional Ruddlesden−Popper $(CH_3(CH_2)_3NH_3)_2(CH_3NH_3)_{n-1}Sn_nI3_{n+1}$ Perovskites. *ACS Energy Lett.* **2017**, *2*, 982−990.
(12) Ren, H.; Yu, S.; Chao, L.; Xia, Y.; Sun, Y.; Zuo, S.; Li, F.; Niu, T.; Yang, Y.; Ju, H.; et al. Efficient and Stable Ruddlesden−Popper Perovskite Solar Cell with Tailored Interlayer Molecular Interaction. *Nat. Photonics* **2020**, *14*, 154−163.
(13) Mitzi, D. B. Synthesis, Crystal Structure, and Optical and Thermal Properties of (C4H9NH3)2MI4 (M = Ge, Sn, Pb). *Chem. Mater.* **1996**, *8*, 791−800.
(14) Stoumpos, C. C.; Cao, D. H.; Clark, D. J.; Young, J.; Rondinelli, J. M.; Jang, J. I.; Hupp, J. T.; Kanatzidis, M. G. Ruddlesden−Popper Hybrid Lead Iodide Perovskite 2D Homologous Semiconductors. *Chem. Mater.* **2016**, *28*, 2852−2867.
(15) Mao, L.; Stoumpos, C. C.; Kanatzidis, M. G. Two-Dimensional Hybrid Halide Perovskites: Principles and Promises. *J. Am. Chem. Soc.* **2019**, *141*, 1171−1190.
(16) Zhang, F.; Lu, H.; Tong, J.; Berry, J. J.; Beard, M. C.; Zhu, K. Advances in Two-Dimensional Organic−Inorganic Hybrid Perovskites. *Energy Environ. Sci.* **2020**, *13*, 1154−1186.
(17) Saparov, B.; Mitzi, D. B. Organic−Inorganic Perovskites: Structural Versatility for Functional Materials Design. *Chem. Rev.* **2016**, *116*, 4558−4596.
(18) Zibouche, N.; Islam, M. S. Structure-Electronic Property Relationships of 2D Ruddlesden-Popper Tin- and Lead-based Iodide Perovskites. *ACS Appl. Mater. Interfaces* **2020**, *12*, 15328−15337.
(19) Cao, D. H.; Stoumpos, C. C.; Farha, O. K.; Hupp, J. T.; Kanatzidis, M. G. 2D Homologous Perovskites as Light-Absorbing Materials for Solar Cell Applications. *J. Am. Chem. Soc.* **2015**, *137*, 7843−7850.
(20) Blancon, J. C.; Stier, A. V.; Tsai, H.; Nie, W.; Stoumpos, C. C.; Traoré, B.; Pedesseau, L.; Kepenekian, M.; Katsutani, F.; Noe, G. T.; et al. Scaling Law for Excitons in 2D Perovskite Quantum Wells. *Nat. Commun.* **2018**, *9*, 2254.
(21) Deng, S.; Shi, E.; Yuan, L.; Jin, L.; Dou, L.; Huang, L. Long-Range Exciton Transport and Slow Annihilation in Two-Dimensional Hybrid Perovskites. *Nat. Commun.* **2020**, *11*, 664.
(22) Hong, X.; Ishihara, T.; Nurmikko, A. V. Dielectric Confinement Effect on Excitons in PbI_4-Based Layered Semiconductors. *Phys. Rev. B* **1992**, *45*, 6961−6964.
(23) Straus, D. B.; Kagan, C. R. Electrons, Excitons, and Phonons in Two-Dimensional Hybrid Perovskites: Connecting Structural, Optical, and Electronic Properties. *J. Phys. Chem. Lett.* **2018**, *9*, 1434−1447.
(24) Gong, X.; Voznyy, O.; Jain, A.; Liu, W.; Sabatini, R.; Piontkowski, Z.; Walters, G.; Bappi, G.; Nokhrin, S.; Bushuyev, O.; et al. Electron−Phonon Interaction in Efficient Perovskite Blue Emitters. *Nat. Mater.* **2018**, *17*, 550−556.
(25) Gao, Y.; Shi, E.; Deng, S.; Shiring, S. B.; Snaider, J. M.; Liang, C.; Yuan, B.; Song, R.; Janke, S. M.; Liebman-Peláez, A.; et al. Molecular Engineering of Organic−Inorganic Hybrid Perovskites Quantum Wells. *Nat. Chem.* **2019**, *11*, 1151−1157.
(26) Seitz, M.; Magdaleno, A. J.; Alcázar-Cano, N.; Meléndez, M.; Lubbers, T. J.; Walraven, S. W.; Pakdel, S.; Prada, E.; Delgado-Buscalioni, R.; Prins, F. Exciton Diffusion in Two-Dimensional Metal-Halide Perovskites. *Nat. Commun.* **2020**, *11*, 2035.
(27) Liu, J.; Xue, Y.; Wang, Z.; Xu, Z.-Q.; Zheng, C.; Weber, B.; Song, J.; Wang, Y.; Lu, Y.; Zhang, Y.; et al. Two-Dimensional CH3NH3PbI3 Perovskite: Synthesis and Optoelectronic Application. *ACS Nano* **2016**, *10*, 3536−3542.
(28) Du, K. Z.; Tu, Q.; Zhang, X.; Han, Q.; Liu, J.; Zauscher, S.; Mitzi, D. B. Two-Dimensional Lead(II) Halide-Based Hybrid Perovskites Templated by Acene Alkylamines: Crystal Structures, Optical Properties, and Piezoelectricity. *Inorg. Chem.* **2017**, *56*, 9291−9302.
(29) Quan, L. N.; Yuan, M.; Comin, R.; Voznyy, O.; Beauregard, E. M.; Hoogland, S.; Buin, A.; Kirmani, A. R.; Zhao, K.; Amassian, A.; et al. Ligand-Stabilized Reduced-Dimensionality Perovskites. *J. Am. Chem. Soc.* **2016**, *138*, 2649−2655.
(30) Billing, D. G.; Lemmerer, A. Synthesis, Characterization and Phase Transitions in the Inorganic-Organic Layered Perovskite-Type Hybrids [(CnH2n+1NH3)2PbI4], n = 4, 5 and 6. *Acta Crystallogr. B* **2007**, *63*, 735−747.
(31) Koh, T. M.; Shanmugam, V.; Guo, X.; Lim, S. S.; Filonik, O.; Herzig, E. M.; Müller-Buschbaum, P.; Swamy, V.; Chien, S. T.; Mhaisalkar, S. G.; et al. Enhancing Moisture Tolerance in Efficient Hybrid 3D/2D Perovskite Photovoltaics. *J. Mater. Chem. A* **2018**, *6*, 2122−2128.
(32) Lemmerer, A.; Billing, D. G. Synthesis, Characterization and Phase Transitions of the Inorganic-Organic Layered Perovskite-Type Hybrids [(C(n)H(2n+1)NH3)2PbI4], n = 7, 8, 9 and 10. *Dalton Trans.* **2012**, *41*, 1146−1157.
(33) Passarelli, J. V.; Fairfield, D. J.; Sather, N. A.; Hendricks, M. P.; Sai, H.; Stern, C. L.; Stupp, S. I. Enhanced Out-of-Plane Conductivity and Photovoltaic Performance in n = 1 Layered Perovskites through Organic Cation Design. *J. Am. Chem. Soc.* **2018**, *140*, 7313−7323.
(34) Maheshwari, S.; Savenije, T. J.; Renaud, N.; Grozema, F. C. Computational Design of Two-Dimensional Perovskites with Functional Organic Cations. *J. Phys. Chem. C* **2018**, *122*, 17118−17122.

https://dx.doi.org/10.1021/acs.jpcc.0c08893
J. Phys. Chem. C 2020, 124, 28201−28209

(35) Gélvez-Rueda, M. C.; Fridriksson, M. B.; Dubey, R. K.; Jager, W. F.; van der Stam, W.; Grozema, F. C. Overcoming the Exciton Binding Energy in Two-Dimensional Perovskite Nanoplatelets by Attachment of Conjugated Organic Chromophores. *Nat. Commun.* **2020**, *11*, 1901.
(36) Kamminga, M. E.; Fang, H.-H.; Filip, M. R.; Giustino, F.; Baas, J.; Blake, G. R.; Loi, M. A.; Palstra, T. T. M. Confinement Effects in Low-Dimensional Lead Iodide Perovskite Hybrids. *Chem. Mater.* **2016**, *28*, 4554−4562.
(37) Marchal, N.; Van Gompel, W.; Gálvez-Rueda, M. C.; Vandewal, K.; Van Hecke, K.; Boyen, H.-G.; Conings, B.; Herckens, R.; Maheshwari, S.; Lutsen, L.; et al. Lead-Halide Perovskites Meet Donor−Acceptor Charge-Transfer Complexes. *Chem. Mater.* **2019**, *31*, 6880−6888.
(38) Plimpton, S. Fast Parallel Algorithms for Short-Range Molecular Dynamics. *J. Comput. Phys.* **1995**, *117*, 1−19.
(39) Mattoni, A.; Filippetti, A.; Saba, M. I.; Delugas, P. Methylammonium Rotational Dynamics in Lead Halide Perovskite by Classical Molecular Dynamics: The Role of Temperature. *J. Phys. Chem. C* **2015**, *119*, 17421−17428.
(40) Maheshwari, S.; Fridriksson, M. B.; Seal, S.; Meyer, J.; Grozema, F. C. The Relation between Rotational Dynamics of the Organic Cation and Phase Transitions in Hybrid Halide Perovskites. *J. Phys. Chem. C* **2019**, *123*, 14652−14661.
(41) Fridriksson, M. B.; Maheshwari, S.; Grozema, F. C. Structural Dynamics of Two-Dimensional Ruddlesden−Popper Perovskites: A Computational Study. *J. Phys. Chem. C* **2020**, *124*, 22096−22104.
(42) Ponder, J. W.; Case, D. A. Force Fields for Protein Simulations. *Adv. Protein Chem.* **2003**, *66*, 27−85.
(43) Breneman, C. M.; Wiberg, K. B. Determining Atom-Centered Monopoles from Molecular Electrostatic Potentials. The Need for High Sampling Density in Formamide Conformational Analysis. *J. Comput. Chem.* **1990**, *11*, 361−373.
(44) Frisch, M. J.; Trucks, G. W.; Schlegel, H. B.; Scuseria, G. E.; Robb, M. A.; Cheeseman, J. R.; Scalmani, G.; Barone, V.; Petersson, G. A.; Nakatsuji, H.; et al. *Gaussian 09*; Rev. A.02, Gaussian: Wallingford, CT, 2016.
(45) Thijssen, J. *Computational Physics*; 2nd edition Cambridge University Press: 2007.
(46) Gálvez-Rueda, M. C.; Peeters, S.; Wang, P.-C.; Felter, K. M.; Grozema, F. C. Effect of Structural Defects and Impurities on the Excited State Dynamics of 2D BA_2PbI_4 Perovskite. *Helv. Chim. Acta* **2020**, *103*, e2000121.

https://dx.doi.org/10.1021/acs.jpcc.0c08893
J. Phys. Chem. C 2020, 124, 28201−28209